ACS NANO

Cite This: ACS Nano 2018, 12, 4812−4823

www.acsnano.org

ARTICLE

Quenching Pathways in $NaYF_4:Er^{3+},Yb^{3+}$ Upconversion Nanocrystals

Freddy T. Rabouw, P. Tim Prins, Pedro Villanueva-Delgado, Marieke Castelijns, Robin G. Geitenbeek, and Andries Meijerink*

Debye Institute for Nanomaterials Science, Utrecht University, Princetonplein 1, 3584 CC Utrecht, The Netherlands

Supporting Information

ABSTRACT: Lanthanide-doped upconversion (UC) phosphors absorb low-energy infrared light and convert it into higher-energy visible light. Despite over 10 years of development, it has not been possible to synthesize nanocrystals (NCs) with UC efficiencies on a par with what can be achieved in bulk materials. To guide the design and realization of more efficient UC NCs, a better understanding is necessary of the loss pathways competing with UC. Here we study the excited-state dynamics of the workhorse UC material β-$NaYF_4$ co-doped with Yb^{3+} and Er^{3+}. For each of the energy levels involved in infrared-to-visible UC, we measure and model the competition between spontaneous emission, energy transfer between lanthanide ions, and other decay processes. An important quenching pathway is energy transfer to high-energy vibrations of solvent and/or ligand molecules surrounding the NCs, as evidenced by the effect of energy resonances between electronic transitions of the lanthanide ions and vibrations of the solvent molecules. We present a microscopic quantitative model for the quenching dynamics in UC NCs. It takes into account cross-relaxation at high lanthanide-doping concentration as well as Förster resonance energy transfer from lanthanide excited states to vibrational modes of molecules surrounding the UC NCs. Our model thereby provides insight in the inert-shell thickness required to prevent solvent quenching in NCs. Overall, the strongest contribution to reduced UC efficiencies in core−shell NCs comes from quenching of the near-infrared energy levels (Er^{3+}: $^4I_{11/2}$ and Yb^{3+}: $^2F_{5/2}$), which is likely due to vibrational coupling to OH^- defects incorporated in the NCs during synthesis.

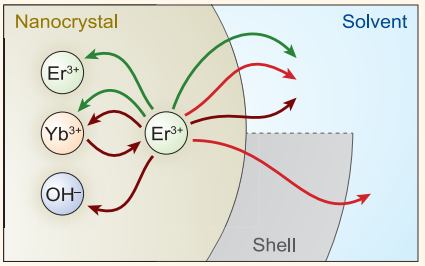

KEYWORDS: *upconversion luminescence, nanocrystals, shell growth, lanthanide ions, surface quenching, excited-state dynamics*

Upconversion (UC) materials are unconventional color-conversion materials that can absorb low-energy and emit higher-energy photons. Examples include polycyclic aromatic hydrocarbons,[1,2] specially designed semiconductor-quantum-dot geometries,[3,4] and crystals doped with lanthanide ions.[5−7] Of particular interest have been β-$NaREF_4$ nanocrystals (NCs; with RE = Y, Gd, or Lu) doped with either Er^{3+} or Tm^{3+} and often co-doped with Yb^{3+} or other lanthanides to increase absorption or tune the emission wavelength.[8−22] Such NCs exhibit narrow-line emissions, and they are photochemically and colloidally stable, making them ideal for background-free biomedical imaging. Moreover, the small size of NCs enables their use in nanoscale designs to enhance the UC luminescence through sensitization[13] or plasmon enhancement.[23−29] However, the efficiency of UC luminescence is significantly lower for nanocrystalline doped $NaREF_4$ than for the corresponding bulk material, because of excited-state quenching by the NC surface and the environment.[10,11,16,19−21,30] The UC efficiency is particularly low in the smallest NCs.[11,14,20]

Efforts have been made to improve the low UC luminescence efficiency of doped $NaREF_4$ NCs. The common strategy to achieve higher efficiencies is to grow inert nonluminescent shells of undoped $NaREF_4$ (with RE = Y, Gd, or Lu) around the doped upconverting core.[11,16] This serves to spatially isolate the active luminescent core from the NC surface and the environment. While this general concept has been well established, a quantitative understanding of UC luminescence quenching in NCs is still lacking. UC in lanthanide-doped crystals is a complicated process, involving (at least) two absorption events, multiple energy-migration and energy-transfer steps, and eventually emission of a high-energy photon. Meanwhile, the efficiency is limited by undesired competing processes such as cross-relaxation, back-transfer, nonradiative decay, and, in the case of NCs, quenching by energy transfer to high-energy vibrations on the surface and/or in the environment of the NCs.[10,11,16,18,22,30] To understand UC luminescence from NCs and minimize quenching requires detailed and quantitative studies that unravel the competition between the various processes at play.

Here, we investigate the quenching mechanisms of the various energy levels involved in UC in $NaYF_4$ NCs co-doped with Er^{3+} and Yb^{3+}, a commonly studied nanocrystalline

Received: February 27, 2018
Accepted: April 12, 2018
Published: April 12, 2018

DOI: 10.1021/acsnano.8b01545
ACS Nano 2018, 12, 4812−4823

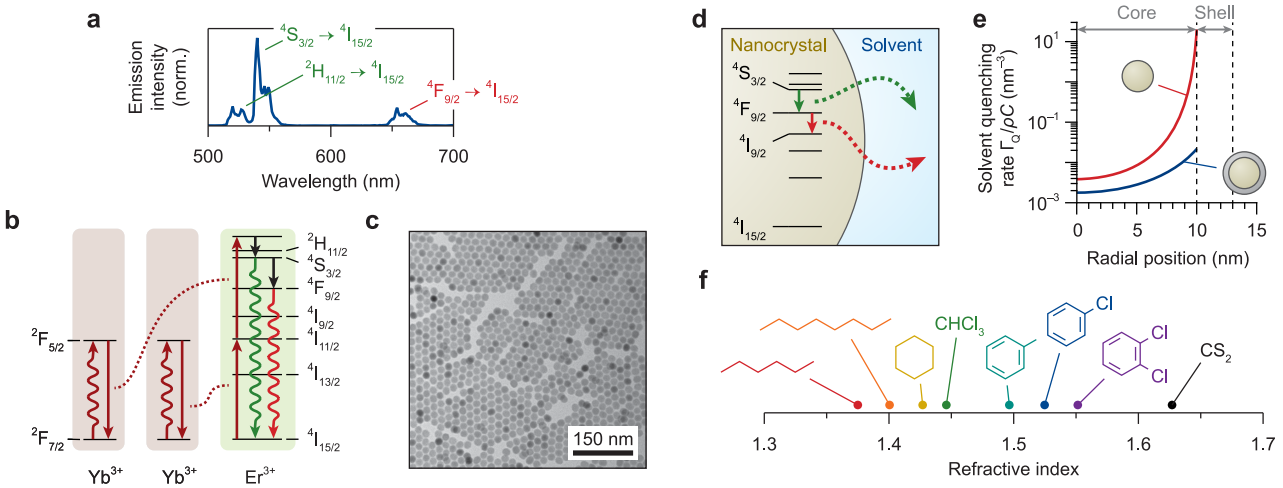

Figure 1. (a) UC emission spectrum of β-$NaYF_4$ nanocrystals co-doped with 2% Er^{3+} and 18% Yb^{3+} dispersed in cyclohexane, upon laser excitation in the Yb^{3+}: $^2F_{7/2} \rightarrow {}^2F_{5/2}$ transition at 980 nm. The nanocrystals emit green photons from the $^2H_{11/2}$ (520 nm) and $^4S_{3/2}$ (540 nm) states and red photons (660 nm) from the $^4F_{9/2}$ state. (b) Upon excitation of Yb^{3+} at 980 nm (dark-red wavy arrows), two consecutive energy-transfer processes (dotted lines) excite an Er^{3+} ion to a high excited state. Subsequently, after one or more nonradiative decay steps (black arrows) Er^{3+} can emit a visible photon (red or green wavy arrows). Other, more complicated, sequences of processes also contribute to the population of visible-emitting states.[35−37] (c) Transmission electron micrograph of the core-only β-$NaYF_4$:0.1% Er^{3+} nanocrystals used in this work. Images of other nanocrystal samples and the extracted size distributions are presented in Figure S1 and Table S1. (d) Schematic of solvent quenching, where an excited state on a lanthanide center (here, Er^{3+}) doped in a nanocrystal can decay by transferring energy to high-energy vibrations in the surrounding solvent. (e) The total rate of solvent quenching by dipole−dipole interaction depends strongly on the radial position of the lanthanide center in the nanocrystal, illustrated here for a nanocrystal of 10 nm radius without (red line) and with (blue line) a 3 nm-thick nonluminescent shell. (f) The range of solvents used in our experiments below, with different chemical nature (affecting the solvent-quenching rate; eq 2) and different refractive index (affecting the radiative decay rate; eq 3).

upconverter showing green and red emissions upon near-infrared excitation.[10,13,14,16,18,20,22] The dynamics of the relevant excited states of Er^{3+} and Yb^{3+} are measured upon direct excitation in NCs with and without shell, with various dopant concentrations, and dispersed in a range of organic solvents with different refractive index and chemical nature. We observe a pronounced dependence of quenching on the chemical nature of the solvent of the NCs (aliphatic *versus* aromatic), pointing to Förster transfer to high-energy solvent vibrations as an important quenching mechanism.[31,32] Solvent quenching affects all energy levels of Er^{3+} involved in near-infrared-to-visible UC, but most notably the red-emitting $^4F_{9/2}$ level. The green emission from the $^2H_{11/2}$ and $^4S_{3/2}$ levels is quenched by cross-relaxation and energy migration at higher Er^{3+} concentrations, while the red emission is hardly affected. The near-infrared levels $^4I_{11/2}$ (Er^{3+}) and $^2F_{5/2}$ (Yb^{3+}) are quenched by coupling to the solvent, by coupling to OH-vibrations of hydroxyl ions incorporated in the crystal structure, and by energy migration to the NC surface. The efficiencies of all quenching pathways are suppressed if the refractive index of the solvent is increased, because this enhances the rates of photon emission but not energy-transfer (*i.e.*, quenching) rates.[33,34] We develop an analytical model for the various quenching pathways, which matches our experimental results and can predict the emission dynamics and efficiencies for NCs of different (quasi-)spherical core−shell geometries and dopant concentrations.

RESULTS

Solvent-Dependent Decay Dynamics. We study the popular UC material β-$NaYF_4$ co-doped with Er^{3+} and Yb^{3+}.[5,8] Upon excitation of Yb^{3+} in the near-infrared absorption band at 980 nm, this material emits green light at 520 and 540 nm and red light at 660 nm (Figure 1a). The conversion of low-energy near-infrared photons to higher-energy visible photons is made possible by successive energy-transfer steps from two (or more) Yb^{3+} ions to Er^{3+}. Both the green and the red UC luminescence can arise after two energy-transfer steps followed by partial nonradiative relaxation (indicated in Figure 1b), although additional pathways involving three energy-transfer steps have been identified leading to red luminescence.[35−37] The energy-transfer processes relevant to UC compete with undesired processes such as (multi)phonon relaxation and cross-relaxation that reduce the UC emission. The spectral characteristics of nanocrystalline β-$NaYF_4$ phosphors with diameters down to sub-10 nm (refs 20 and 50) are similar to those of bulk β-$NaYF_4$, but the emission efficiencies are significantly lower.[10,11,19−21,30] In this work we systematically study the energy-loss pathways in UC NCs (Figure 1c, Figure S1 and Table S1) that lead to these lower efficiencies, as a function of the dopant concentration, for core-only and core−shell geometries and for NCs dispersed in a range of solvents.

Previous studies have identified that the environment of lanthanide-doped NCs, most notably the solvent, affects luminescence quenching.[10,11,18,22,30] It is not always realized that such quenching is a form of Förster energy transfer, by dipole−dipole coupling of an electronic transition of a lanthanide dopant to vibrations of the solvent and ligand molecules (Figure 1d).[38] The rate of energy transfer by dipole−dipole coupling, γ_{ET}, scales with the inverse sixth power of the separation between the energy donor (the luminescent center) and the energy acceptor (the solvent vibration):

$$\gamma_{ET}(\mathbf{r}_0, \mathbf{r}) = \frac{C}{|\mathbf{r} - \mathbf{r}_0|^6} \quad (1)$$

where $\mathbf{r}_0$ and $\mathbf{r}$ are the positions of the donor and acceptor, respectively. The parameter C is the "energy-transfer strength" prefactor, the value of which depends on the energy match of

DOI: 10.1021/acsnano.8b01545
ACS Nano 2018, 12, 4812−4823

transitions in the lanthanide center to the vibrational energies of the solvent[31,32,38] as well as on the oscillator strengths of the donor and acceptor transitions involved.[43] The total solvent-quenching rate Γ_Q experienced by a luminescent center is determined by its dipole−dipole coupling to all solvent vibrations surrounding the NC, which depends on the diameter of the NC and on the location of the center inside the NC. If we assume that the NC is spherical with an outer radius a_{out}, we obtain a simple expression by integrating eq 1 over all solvent molecules outside the NC:

$$\Gamma_Q(r_0, \rho C) = \int_{V_{out}} \gamma_{ET}(\mathbf{r}_0, \mathbf{r})\rho d\mathbf{r} = \frac{4\pi\rho C a_{out}^3}{3(a_{out}^2 - r_0^2)^3} \quad (2)$$

where V_{out} is the volume occupied by solvent, $r_0 = |\mathbf{r}_0|$ is the radial position of the Er^{3+} center, and ρ is the density of solvent vibrations involved in quenching. Interestingly, the amount of quenching depends only on the geometry of the NC (outer radius a_{out} and radial position r_0 of the dopant) and on the "quenching density" ρC—the product of the density of vibrations and the energy-transfer strength; units of volume per time—that describes the interaction with the solvent. To avoid that the quenching rate Γ_Q becomes infinite at the surface of core-only NCs ($r_0 = a_{out}$ in eq 2), we assume throughout this article that the "outer radius" a_{out} (beyond which volume is occupied by solvent) is 0.3 nm larger than the physical radius of the NC as determined by electron microscopy. This 0.3 nm separation can be justified if one realizes that this space of approximately one atom thickness is occupied by species contributing significantly less to vibrational quenching than the solvent does, for example, fluoride anions of the host crystal or headgroups of the ligands (in our experiments, carboxylate head groups of oleate). The solvent-quenching model could be further fine-tuned, at the cost of increased complexity, by considering that the NC can be covered by long-chain organic ligands (in our experiments below, oleic acid) that occupy most of the volume up to 1−1.5 nm distance from the NC surface. Here, we approximate the combination of ligand and solvent as one continuous medium that can be described with a single quenching density ρC. In Figure 1e we plot the solvent-quenching rate normalized to the quenching density $\Gamma_Q/\rho C$. We see that the solvent-quenching rate differs by orders of magnitude between luminescent centers near the surface and those near the center of a core-only NC (red line). Growing a shell of 3 nm thickness can suppress the solvent-quenching rate by a factor 2−1000, depending on the location of a center in the NC (blue line). These pronounced effects of geometry on the quenching rate are manifestations of the strong distance dependence of dipole−dipole coupling. Our model can predict the distribution of solvent quenching rates for any spherical NC geometry (core-only or core−shell) if the quenching density ρC of a particular solvent to a particular dopant's excited state is known.

In addition to inducing nonradiative quenching, the solvent—through its refractive index n—also affects the radiative decay rate Γ_{rad} of dopant centers in NCs:[33,34]

$$\Gamma_{rad}(n) = \frac{\Gamma_{rad}^{bulk}}{n}\left(\frac{3n^2}{2n^2 + n_{NC}^2}\right)^2 \quad (3)$$

where Γ_{rad}^{bulk} is the radiative decay rate in a bulk sample, and n_{NC} is the refractive index of the NC material [here, $n_{NC} = 1.48$ (ref 39)]. This effect is the same for all luminescent centers inside a NC independent of their exact location, if the NC is (quasi-)spherical and much smaller than the emission wavelength. We measured the values of Γ_{rad}^{bulk} for each relevant level on a bulk microcrystalline sample (Figure S2). From these reference values we can calculate the radiative decay rate in any solvent, if we know its refractive index. Throughout this article we will use tabulated refractive indices in the visible, neglecting that they are in fact slightly lower (by at most 0.02 point) in the infrared where the excited states emit (partially). This translates into an acceptable error of <1% in the calculated radiative decay rates in NCs. The series of solvents used in our experiments (Figure 1f) covers a range of refractive indices from $n = 1.375$ (hexane) to $n = 1.627$ (carbon disulfide). This corresponds to a 40% variation in radiative decay rate (eq 3). Importantly, however, the solvents are different not only in terms of refractive index but also chemically. The chemical nature of the solvent affects its vibrational spectrum and thereby the dipole−dipole coupling to various Er^{3+} transitions. We will see below that resonances of the C−H stretch vibrational energy with transitions on the Er^{3+} ion affect the strength of solvent quenching. Hence, solvent effects manifest as changes in the radiative decay of lanthanide dopants in NCs (through n in eq 3) as well as in nonradiative quenching (through ρC in eq 2).

The total decay rate Γ_{tot} of a luminescent center in a nanocrystal is the sum of the rates of all available decay pathways:

$$\Gamma_{tot} = \Gamma_{rad}(n) + \Gamma_Q(r_0, \rho C) \quad (4)$$

where we have written explicitly that the radiative decay rate Γ_{rad} depends on the solvent refractive index n and that the solvent-quenching rate Γ_Q depends on the radial coordinate r_0 of the center in the NC and on the quenching density ρC of the solvent. For now we assume that Γ_{rad} and Γ_Q are the only decay pathways for the luminescent centers. Assuming that the dopant centers are homogeneously distributed within the NC (which may in fact be not exactly true),[40] we obtain the expected decay dynamics of an ensemble of doped NCs by integrating Γ_Q over the NC volume:

$$I(t) = V^{-1}\int_0^a e^{-\Gamma_{tot}t} 4\pi r_0^2 dr_0 = R(t)Q(t) \quad (5)$$

where a and V are the radius and volume of the luminescent core of the NC, respectively,

$$R(t) = e^{-\Gamma_{rad}(n)t} \quad (6)$$

is the monoexponential radiative decay component (eq 3), and

$$Q(t) = V^{-1}\int_0^a e^{-\Gamma_Q(r_0,\rho C)t} 4\pi r_0^2 dr_0 \quad (7)$$

is the multiexponential solvent-quenching component to the decay (eq 2).

As we will see below, the decay dynamics of luminescent centers in NCs are accurately described by eq 5 in many cases. In other cases, at higher doping concentrations, additional decay processes become active. One of these is energy migration, that is, hopping of the excited-state energy from center to center. The effect of energy migration on the excited-state dynamics will become apparent in our experimental data. This is however difficult to take into account quantitatively with our microscopic model, because the microscopic rate distributions (*e.g.*, for solvent quenching) are correlated for neighboring ions involved in energy migration. In this work we

DOI: 10.1021/acsnano.8b01545
ACS Nano 2018, 12, 4812−4823

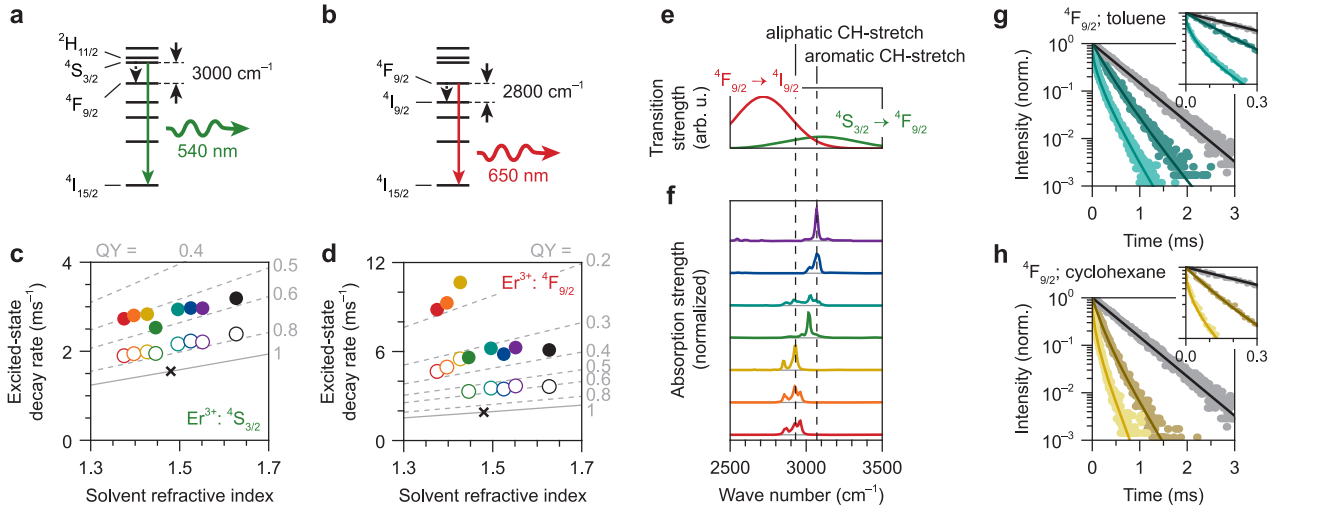

Figure 2. (a) Energy-level scheme of Er^{3+} with the green emission from the $^4S_{3/2}$ level (in thermal equilibrium with $^2H_{11/2}$; ref 44) indicated as a green arrow and the nonradiative transition to the $^4F_{9/2}$ level as a black dashed arrow. (b) Same for the red emission from the $^4F_{9/2}$ level and the competing nonradiative transition to the $^4I_{9/2}$ level. (c) Average excited-state decay rates $\langle\Gamma_{tot}\rangle$ of the green-emitting level in $NaYF_4$:0.1% Er^{3+} NCs dispersed in different solvents (different colors; see Figure 1f), compared to the decay rate in bulk $NaYF_4$:0.1% Er^{3+} (black cross). Filled circles represent core-only NCs, open circles core−shell NCs. Gray lines are iso-quantum-yield contours plotting $\eta \approx \Gamma_{rad}(n)/\langle\Gamma_{tot}\rangle$ with $\Gamma_{rad}(n)$ according to eq 3. (d) Same, but for the red-emitting level. (e) The emission line shapes of the $^4S_{3/2} \rightarrow {}^4F_{9/2}$ (green) and the $^4F_{9/2} \rightarrow {}^4I_{9/2}$ (red) transitions of Er^{3+}, which are responsible for nonradiative decay of the green- and red-emitting levels (see panel a), estimated based on the data from ref 45. (f) Infrared absorption spectra of hexane (red), octane (orange), cyclohexane (yellow), chloroform (green), toluene (cyan), chlorobenzene (blue), and *o*-dichlorobenzene (purple), taken from the SDBS database of the National Institute of Advanced Industrial Science and Technology (AIST), Japan. Dashed lines indicate the approximate spectral position of the C-H stretch vibrational energy in aliphatic (~2930 cm^{-1}) and aromatic (~3070 cm^{-1}) molecules. (g) Photoluminescence decay curves of the red-emitting $^4F_{9/2}$ level upon direct excitation in bulk $NaYF_4$:0.1% Er^{3+} (gray), compared to core−shell NCs (dark cyan) and core-only NCs (light cyan) of the same composition dispersed in toluene. The inset shows a zoom-in of the first 0.3 ms. Solid lines are fits to the solvent-quenching model (eq 5). (h) Same, but comparing bulk to NCs dispersed in cyclohexane.

will therefore discuss the effects of energy migration qualitatively. Another process relevant at high dopant concentrations is cross-relaxation, in which a luminescent center transfers part of its energy to neighbors. The effect of this on the excited-state dynamics of the donor center can be taken into account analytically.[41,42] We use that the rate of cross-relaxation energy transfer by dipole−dipole interaction depends on the inverse sixth power of the distance r_{da} between a donor center and an acceptor center. Including this pathway adds a cross-relaxation term $\Gamma_X = \sum_a C_X/r_{da}^6$ (where prefactor C_X describes the "cross-relaxation strength", and the summation runs over all nearby acceptor centers) to the total decay rate of a donor center (eq 4). To consider all possible local electronic environments of a luminescent center, that is, its separation from nearby acceptor centers, we have to take into account the complicated crystal structure of our β-$NaYF_4$ NCs that has two types of cation sites for rare-earth ions (Y^{3+} or luminescent dopants), one of which is only 50% occupied.[5] If we assume a homogeneous dopant distribution and neglect finite-size effects in the NC,[33] then the local electronic environment of a luminescent center (determining Γ_X) is uncorrelated with its radial position (determining Γ_Q). Under this assumption, the total decay including solvent quenching and cross-relaxation can be written as

$$I(t) = R(t)Q(t)X(t) \tag{8}$$

where the multiexponential factor $X(t)$ in β-$NaYF_4$ NCs reads as

$$X(t) = \frac{2}{3}\left[\prod_i (1 - \phi + \phi e^{-C_X t/r_i^6})^{n_i} \times \prod_i \left(1 - \frac{\phi}{2} + \frac{\phi}{2} e^{-C_X t/r_i^{*6}}\right)^{n_i^*}\right] + \frac{1}{3}\left[\prod_i \left(1 - \frac{\phi}{2} + \frac{\phi}{2} e^{-C_X t/r_i^6}\right)^{n_i} \times \prod_i (1 - \phi + \phi e^{-C_X t/r_i^{*6}})^{n_i^*}\right] \tag{9}$$

where ϕ is the doping concentration of acceptor centers, that is, the fraction of nonluminescent host cations substituted, and the products run over the (next-)nearest-neighbor shells as determined by the host-crystal structure. This long expression with four products explicitly considers the two different rare-earth cation sites in β-$NaYF_4$, in terms of the neighborlist r_i, n_i (refs 33, 41, and 42) for like sites and r_i^*, n_i^* for unlike sites. In some of our NCs studied below, cross-relaxation takes place with both Er^{3+} and Yb^{3+} dopants as energy acceptors. The total decay function for this situation becomes

$$I(t) = R(t)Q(t)X_{Er}(t)X_{Yb}(t) \tag{10}$$

where each factor $X_i(t)$ (i = Er, Yb) is a function as in eq 9 with $\phi = \phi_i$ and $C_X = C_{X,i}$. Here we neglect correlations in the distribution of cross-relaxation rates to Er^{3+} neighbors and those to Yb^{3+} neighbors, which is justified at relatively low doping concentrations. Such correlations become important at the highest doping concentrations, because for any one excited dopant center, the cross-relaxation rates are determined by the occupation of nearby cation sites, which can each contain (apart from an inert Y^{3+} ion) an Yb^{3+} acceptor, or an Er^{3+} acceptor, but not both at the same time.

DOI: 10.1021/acsnano.8b01545
ACS Nano 2018, 12, 4812−4823

We note that all nonradiative decay processes considered here—solvent quenching, cross-relaxation, and energy migration—are manifestations of Förster resonance energy transfer by dipole−dipole coupling. For solvent quenching, an excited lanthanide ion in the NC is the energy donor and a vibrational mode in a solvent molecule is the energy acceptor, while for cross-relaxation and energy migration the donor and acceptor are both lanthanide ions. Dipole−dipole coupling has a strong distance dependence scaling with the donor−acceptor distance to the inverse sixth power. This, combined with the random distribution of luminescent dopants in a (nano)crystal, determines the multiexponential nature of the decay dynamics. The dipole−dipole coupling rate also depends on the spectral overlap between the donor transition (*i.e.*, its emission spectrum) and the acceptor transition (*i.e.*, its absorption spectrum), as we will discuss below. Importantly, the *efficiency* of dipole−dipole coupling—the rate of coupling compared to other decay processes of the donor, such as radiative decay—depends on the oscillator strength of the acceptor transition.[43] Since f−f transitions of lanthanide dopants are parity-forbidden, the dipole−dipole coupling to lanthanide acceptors is weak and therefore short-range (Å−nm). This is why cross-relaxation and energy migration are negligible except at higher doping concentrations, when the average distance between dopants is of the order of a nm or less. Many vibrational transitions of organic molecules, on the other hand, are dipole-allowed. As a result, the coupling of a luminescent dopant in a NC to a molecule of the surrounding solvent can be significant, even if the separations are as large as 1−10 nm.

Solvent Quenching of the Visible Emissions. We focus first on the dynamics of the green-emitting [$^4S_{3/2}$; in thermal equilibrium with $^2H_{11/2}$ (ref 44); Figure 2a] and red-emitting ($^4F_{9/2}$; Figure 2b) levels in $NaYF_4$ NCs doped with 0.1% Er^{3+}. In these NCs the interactions between Er^{3+} centers, for example, cross-relaxation or energy migration, are expected to be negligible because the average ion−ion separation is large at low dopant concentrations. The decay dynamics of these levels are multiexponential (Figure S3), signifying that nonradiative decay rates vary among the Er^{3+} centers as expected in the case of solvent quenching (Figure 1e). As a first simple analysis, we extract the average excited-state decay rates $\langle\Gamma_{tot}\rangle$ of the green-emitting (Figure 2c) and red-emitting (Figure 2d) levels from single-exponential fits, comparing core-only NCs (filled circles) and core−shell NCs (open circles) in different solvents (colors) to bulk material (black cross). The decay rates in core-only and core−shell NCs (circles) are faster than the decay rate in bulk (cross) for both levels and for all solvents, confirming the presence of nonradiative quenching pathways in NCs. Indeed, the energy gap from both the green- and red-emitting level to the next-lower-energy level is approximately 3000 cm^{-1} (Figure 2a,b), which can be bridged by coupling to vibrations in organic molecules, such as the C−H stretch vibration. From the fitted decay rates $\langle\Gamma_{tot}\rangle$ and eq 3 we can estimate the average quantum yield $\eta \approx \Gamma_{rad}/\langle\Gamma_{tot}\rangle$ of the Er^{3+} excited states in NCs, as indicated by the gray "iso-quantum-yield" contours in Figure 2c,d.[34] The quantum yields are approximately 55% (75%) for the green-emitting levels in core-only (core−shell) NCs and 15−40% (30−60%) for the red-emitting level in core-only (core−shell) NCs. Clearly, the green emission is quenched less than the red emission. Furthermore, the growth of a nonluminescent shell suppresses quenching, as expected from Figure 1e.[11,19,20]

If the Er^{3+} excited states in NCs underwent some quenching mechanism independent of the surrounding solvent, we would observe decay rates $\Gamma_{tot}(n) = \Gamma_{rad}(n) + \Gamma_{nr}$ (with a constant nonradiative component Γ_{nr}) that steadily increase with increasing solvent refractive index n. More precisely, the dependence would be approximately linear for refractive indices close to the bulk value (from a series expansion of eq 3):

$$\Gamma_{tot}(n) \approx \Gamma_{rad}^{bulk} + \Gamma_{nr} + \frac{7\Gamma_{rad}^{bulk}}{3n_{NC}}(n - n_{NC}) \quad (11)$$

if Γ_{nr} is not affected by the nature of the solvent. For the green-emitting level we observe this approximately linear increase in decay rate with refractive index (Figure 2c), but the decay rate in chloroform (green) is noticeably slower. For the red-emitting level the trend in decay rate as described by eq 11 is not apparent (Figure 2d). Instead, the decay rates in the aliphatic solvents [hexane (red), octane (orange), cyclohexane (yellow)] are nearly a factor of 2 faster than in the other solvents and even faster than in water.[18] In fact the difference between the organic solvents considered here is so large that quenching of the red emission in core−shell NCs dispersed in aliphatic solvents is similar to quenching of core-only NCs in the aromatic solvents.

We can qualitatively understand this difference in quenching rate between aliphatic and aromatic solvents by considering their vibrational energy spectra. The highest-energy vibrational modes in hydrocarbon molecules are CH-stretch modes with energies around 3000 cm^{-1}. This nearly matches the energies of the $^4S_{3/2} \rightarrow {}^4F_{9/2}$ and $^4F_{9/2} \rightarrow {}^4I_{9/2}$ transitions of Er^{3+} (Figure 2e),[45] which are involved in the nonradiative decay of the green- and red-emitting levels. Since we interpret solvent quenching as dipole−dipole coupling between the excited Er^{3+} ion and solvent vibrations, the coupling strength should scale with the oscillator strength of the vibrational mode, the oscillator strength of the relevant Er^{3+} transition, and its spectral overlap of the vibrational mode with the Er^{3+} transition.[43] Indeed, the oscillator strength of the $^4F_{9/2} \rightarrow {}^4I_{9/2}$ transition is approximately 5× larger than that of the $^4S_{3/2} \rightarrow {}^4F_{9/2}$ transition [2.79×10^{-7} *versus* 6.32×10^{-8} (ref 45)], consistent with the 4−10× faster solvent quenching (depending on the solvent; Figure 2c,d and Figure S3). More importantly, the significantly stronger quenching of the red emission in aliphatic solvents than in aromatic solvents is explained by the energy resonance of the $^4F_{9/2} \rightarrow {}^4I_{9/2}$ transition with the CH-stretch vibrational spectra of the solvents (Figure 2f). While the aliphatic solvents (CH-stretch at ∼2930 cm^{-1}) have good spectral overlap with the $^4F_{9/2} \rightarrow {}^4I_{9/2}$ transition resulting in strong quenching, the aromatic solvents (CH-stretch at ∼3070 cm^{-1}) have less overlap resulting in weaker quenching.

Based on these clear indications of solvent-related quenching confirming results from previous studies,[10,11,18,22,30] we use the solvent-quenching model introduced above (eq 5) to quantify the quenching behavior in the different solvents. As illustrative examples, we analyze the decay dynamics of the red emission from $NaYF_4$:0.1% Er^{3+} NCs dispersed in aromatic toluene (Figure 2g) and in aliphatic hexane (Figure 2h). Figure S3 shows the results for other solvents and for the green emission. We compare core-only NCs (lighter colors) to core−shell NCs (darker colors) and bulk material (gray). The decay dynamics in NCs are clearly multiexponential, while those in the bulk material are not. The solvent-quenching model (solid lines)

DOI: 10.1021/acsnano.8b01545
ACS Nano 2018, 12, 4812−4823

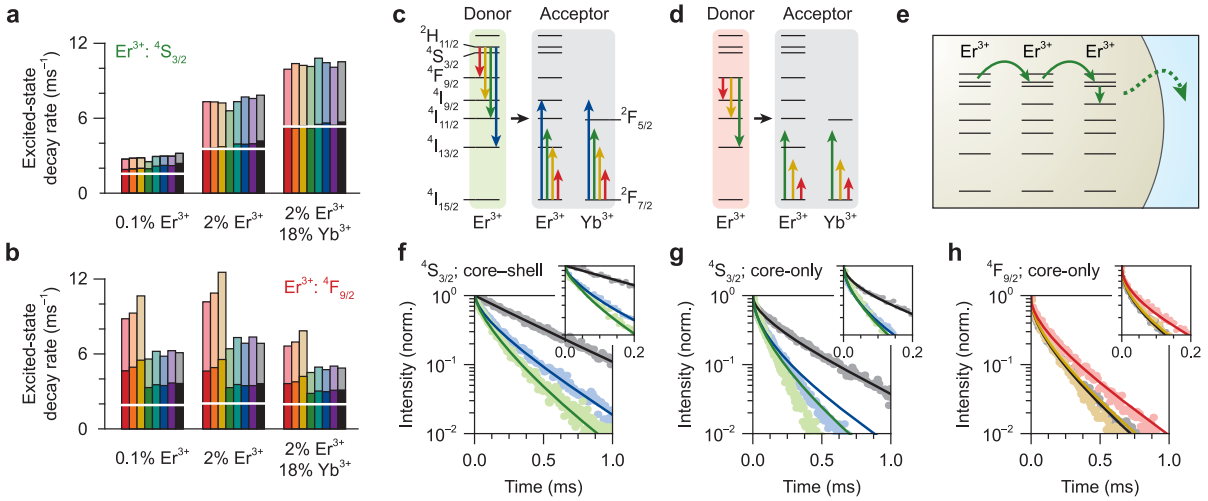

Figure 3. (a) The average decay rate of the green-emitting level $^4S_{3/2}$ for core–shell NCs (dark-colored bars) and core-only NCs (light-colors bars) with different doping concentrations (as indicated) and dispersed in different solvents (different colors), obtained from a single-exponential fit to the decay dynamics. White horizontal lines indicate the corresponding average decay rate in the bulk material. (b) Same for the red-emitting level $^4F_{9/2}$. (c) Possible cross-relaxation pathways from the green-emitting levels of Er^{3+} to neighboring Er^{3+} or Yb^{3+} ions in the ground state. (d) Same for the red-emitting level of Er^{3+}, where all of the possible cross-relaxation pathways exhibit a large energy mismatch between the donor and acceptor transition. (e) Schematic representation of energy migration (*i.e.*, hopping) among Er^{3+} ions to the NC surface. (f) Photoluminescence decay curves of the green Er^{3+} emission in core–shell NCs dispersed in toluene, with doping concentrations of 0.1% Er^{3+} (black), 2% Er^{3+} (blue), and 2% Er^{3+} + 18% Yb^{3+} (green). Solid lines are fits to our model including solvent quenching and cross-relaxation (eqs 8 and 10). The inset shows a zoom-in on the first 0.2 ms. (g) Same for the green emission from core-only NCs. (h) Same for the red emission from core-only NCs, doped with 0.1% Er^{3+} (black), 2% Er^{3+} (yellow), and 2% Er^{3+} + 18% Yb^{3+} (red).

matches this multiexponential behavior very well using the quenching density ρC as the only fit parameter. More precisely, the reduced χ^2 parameters representing the fit quality are 1.22 ± 0.08 for green emission from core-only NCs, 1.08 ± 0.05 for green emission in core–shell NCs, 1.56 ± 0.19 for red emission from core-only NCs, and 1.26 ± 0.16 for red emission in core–shell NCs (mean ± standard deviation over eight solvents; Figure S3). The solvent-quenching model captures the effect of shell growth particularly well,[11,19,20] as evidenced by the very similar values for ρC fitted on the core-only and core–shell dynamics (Figure S3d,h). This means that, if the quenching density ρC is known for a particular dopant excited state in a particular solvent, the model can predict the solvent-quenching behavior for any (quasi-)spherical core–shell NCs, or even—with adaptations—for other shapes.[46] For example, the model predicts that a 9 nm inert shell is required to suppress solvent quenching of the green luminescence from 20 nm-diameter NCs in hexane and achieve higher than 95% luminescence quantum yield (at low doping concentration, in the limit of negligible cross-relaxation), while it requires a 20 nm shell to achieve the same for the red luminescence (Figure 5).

Ion–Ion Interactions at Higher Doping Concentrations. While NCs doped at low concentrations of 0.1% are ideal to study the fundamentals of solvent quenching, NCs must be doped at higher concentrations to achieve optimal UC efficiencies.[47] The average dopant–dopant separations are shorter, thus enhancing the rates and efficiencies of a variety of energy-transfer processes. These include the various energy-transfer processes that are necessary to achieve UC, but also undesired energy-loss pathways such as cross-relaxation and energy migration to the NC surface. The UC brightness and efficiency are determined by a subtle balance between the impact of these different energy-transfer processes.

Figure 3a shows the average decay rate (from a simple single-exponential fit to the dynamics) of the green emitting level in NCs with different doping concentrations: 0.1% Er^{3+} (left), 2% Er^{3+} (middle), and 2% Er^{3+} + 18% Yb^{3+} (right). The decay rates increase significantly going from the low-doped sample to the higher doping concentrations, both in NCs (colored bars) and in the bulk material (white line). This is mostly the result of cross-relaxation, which occurs between dopant centers at typical separations of 1 nm and closer[42] and is therefore similar in 20 nm-diameter NCs to bulk material. However, we also see that the absolute difference in decay rate between core-only (dark-colored bars) and core–shell NCs (light-colored bars) increases with increasing Er^{3+} concentration. This signifies that the surface-related contribution to the total decay becomes stronger. We ascribe this to energy migration from Er^{3+} to Er^{3+} ion within the NC, which allows the excited-state energy to reach the NC surface where it is quenched rapidly by solvent vibrations (Figure 3e). Migration becomes stronger at higher Er^{3+} concentrations (compare 0.1% Er^{3+} and 2% Er^{3+}), but its effect on the decay of the green luminescence is minimized when the energy can no longer reach the surface (compare core-only and core–shell).

Surprisingly, the decay dynamics of the red emission do not accelerate with increasing dopant concentrations, neither in $NaYF_4$ NCs nor in the bulk material (Figure 3b). Hence, while the green-emitting levels are quenched by cross-relaxation and energy migration, the red-emitting level is not. In fact, the quenching seems to *decrease* for the highest dopant concentrations, but this is an artifact due to the slightly larger sizes of our highly doped NCs (21.6 nm *versus* ~19 nm diameter for the lower concentrations; Table S1), resulting in reduced solvent quenching. We can understand why cross-relaxation has a stronger effect on the green-emitting level than on the red-emitting level from the energy-level structures of Er^{3+} and Yb^{3+} (Figure 3c,d). Near-perfect energy matching is possible for cross-relaxation from the green-emitting levels of Er^{3+} to neighboring Er^{3+} ions in the ground state (blue and

DOI: 10.1021/acsnano.8b01545
ACS Nano 2018, 12, 4812–4823

yellow arrows in Figure 3c), and a small mismatch exists for cross-relaxation to a neighboring ground-state Yb^{3+} ion (blue arrows). In contrast, possible cross-relaxation pathways of the red-emitting level of Er^{3+} all exhibit a larger energy mismatch (Figure 3d) and should therefore be significantly less efficient. This is consistent with previous studies on bulk $NaYF_4$ crystals doped with Er^{3+}.[6]

To more quantitatively analyze the quenching dynamics in $NaYF_4$ NCs doped with high concentrations of Er^{3+} and Yb^{3+}, we fit the photoluminescence decay dynamics to our full model including radiative decay, solvent quenching, and cross-relaxation (eq 8 for NCs doped with only Er^{3+} or eq 10 for NCs co-doped with Er^{3+} and Yb^{3+}). Figure 3f shows the decay of the green emission in core−shell NCs dispersed in toluene and doped with 0.1% Er^{3+} (black), 2% Er^{3+} (blue), or co-doped with 2% Er^{3+} and 18% Yb^{3+} (green). In modeling the experimental data, we introduce only two new fit parameters, the cross-relaxation strengths C_{Er} and C_{Yb}, while keeping the other parameters fixed based on the solvent-quenching analysis above (see Figure 2). Our model (solid lines) matches the experimental data very well using fit parameters $C_{Er} = 9.8 \times 10^5$ $Å^6$ ms^{-1} and $C_{Yb} = 3.2 \times 10^3$ $Å^6$ ms^{-1} (see Figure S4 for fit results for the other solvents). This corresponds to a critical Förster radius $R_0 = \sqrt[6]{C_{Er,Yb}/\Gamma_{rad}}$ of 9.2 Å for Er^{3+}−Er^{3+} cross-relaxation, a typical value for Förster transfer to a lanthanide acceptor.[42,51] For Er^{3+}−Yb^{3+} cross-relaxation we obtain 3.5 Å, somewhat shorter because of the energy mismatch for this pathway (Figure 3c). Alternatively, we can calculate a rate of 308 ms^{-1} for cross-relaxation from the green-emitting levels ($^2H_{11/2}$ and $^4S_{3/2}$) to a nearest-neighbor Er^{3+} ion or 1.0 ms^{-1} to a nearest-neighbor Yb^{3+} ion, compared to a radiative decay rate of 1.6 ms^{-1} for NCs in toluene. Figure S5 confirms that quenching of the green emission at high Er^{3+} concentration is mainly due to cross-relaxation, not for example energy migration to the surface,[21] because we can perfectly reproduce the experimental decay curves from bulk $NaYF_4$ doped with high Er^{3+} concentration assuming only radiative decay and cross-relaxation, with all parameters fixed. This also confirms that the distribution of donor−acceptor distances, which determines the cross-relaxation rates, in our NCs is similar to bulk material. Hence, if our NCs show deviations from a statistical distribution of dopant ions as reported by Dong *et al.*,[40] these are not strong enough to affect the interactions between dopants significantly.

The effect of concentration quenching due to energy migration becomes apparent from the green emission dynamics from core-only NCs (Figure 3g). Our model, using the fit parameters for solvent quenching and cross-relaxation we have determined before, matches the emission dynamics shortly after the laser pulse well (inset). At later times ($t > 0.2$ ms) the experimental decay from NCs with high Er^{3+} doping (blue and green) is clearly faster than the model predicts. This is the result of energy migration, which provides a decay pathway for the excited Er^{3+} dopants in the NC center (Figure 3e) that would otherwise decay slowly. Energy migration from Er^{3+} to Er^{3+} can occur also in core−shell NCs. However, the effect on the emission dynamics is less significant (Figure 3f), because the undoped shell prevents migration to the NC surface. This means that our model of solvent quenching plus cross-relaxation can accurately predict the dynamics and quantum yield of green Er^{3+} emission at high dopant concentrations in core−shell NCs, but will overestimate the green-emission quantum yield in core-only NCs. Modeling the effect of energy migration quantitatively is beyond the scope of this article, but can be an interesting follow-up work.

The decay dynamics of the red emission from core-only NCs at high dopant concentrations (Figure 3h) are accurately predicted by the solvent-quenching model (eq 5; quenching density ρC fixed) without introducing cross-relaxation as an additional decay pathway. A small deviation between experiment and model at late times indicates that some concentration quenching and energy migration takes place in the red (*i.e.*, among $^4F_{9/2}$ levels), but weaker than in the green (*i.e.*, among $^2H_{11/2}$ and $^4S_{3/2}$ levels). This modeling of the red emission dynamics is consistent with our earlier conclusion that the red emission is hardly affected by cross-relaxation or energy migration.

Quenching of the Infrared Emissions. We now turn our attention to the near-infrared energy levels of Er^{3+} ($^4I_{11/2}$) and Yb^{3+} ($^2F_{5/2}$). Figure 4a shows the average decay rate (from a simple single-exponential fit) of the near-infrared emission (~1000 nm) from the Er^{3+} $^4I_{11/2}$ level in NCs doped with 2% Er^{3+}. The decay rates, depending on the solvent, are approximately 1 ms^{-1} for core−shell NCs (open circles) and 6 ms^{-1} for core-only NCs (filled circles), compared to 0.13 ms^{-1} in the bulk material (at 0.1% Er^{3+}; Figure S2). This means that the $^4I_{11/2}$ level is strongly quenched in NCs, to ~10% quantum yield for core−shell NCs and ~2% quantum yield for core-only NCs. Quenching by cross-relaxation to neighboring Er^{3+} ions can be excluded, because the energy-level structure of Er^{3+} makes energy-conserving cross-relaxation pathways impossible (see also Figure S6). The quenching of core-only NCs is somewhat dependent on the chemical nature of the solvent, with the aliphatic solvents showing slightly faster decay rates and chloroform showing a slower decay rate. However, for core−shell NCs the linear refractive index dependence of decay rates indicates a solvent-independent nonradiative component (eq 11). Moreover, the solvent-quenching model fails to reproduce the decay dynamics of the Er^{3+} near-infrared emission in core-only and core−shell NCs with a single value for the quenching density (Figure 4b). We propose therefore that the major contributor to quenching of the near-infrared-emitting Er^{3+} level, especially in core−shell structures, is energy transfer to OH-vibrations. Indeed, the vibrational energy of approximately 3500 cm^{-1} precisely matches the $^4I_{11/2}$−$^4I_{13/2}$ energy gap, thus explaining why quenching is strong. OH^- ions likely substitute some native F^- sites of the NC during the synthesis, where NaOH is used as a Na^+ source. Indeed, preventing the inclusion of oxygen in $NaYF_4$ crystals is notoriously difficult.[5] New synthesis procedures[20] using Na-oleate instead of NaOH as Na^+ source can potentially prevent this and thus suppress quenching of the Er^{3+} $^4I_{11/2}$ level.

Figure 4c shows the average decay rate of the near-infrared emission from Yb^{3+} in NCs doped with various dopant concentrations, comparing core-only to core−shell NCs. NCs doped with 0.1% Yb^{3+}, with either core-only or core−shell geometry, show mainly radiative decay with a rate close to that in the bulk material. We conclude from this that solvent quenching by dipole−dipole coupling is negligible for the $^2F_{5/2}$ excited state, and we can therefore not use the solvent-quenching model. This was to be expected, because Yb^{3+} is effectively a two-level system with an energy gap of approximately 10,000 cm^{-1}, that is, over three times the highest vibrational energy in hydrocarbon molecules. At higher doping concentrations the Yb^{3+} decay is faster and strongly

DOI: 10.1021/acsnano.8b01545
ACS Nano 2018, 12, 4812−4823

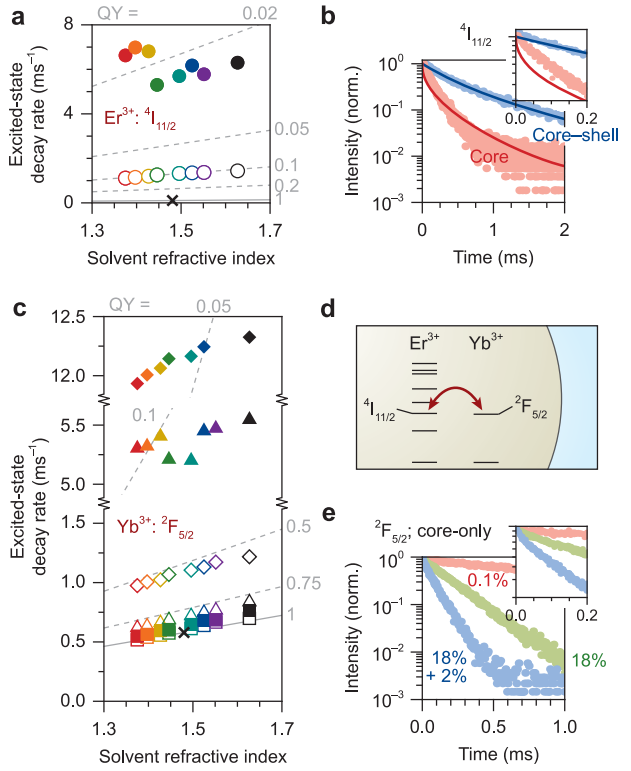

Figure 4. (a) Average decay rates $\langle\Gamma_{tot}\rangle$ of the near-infrared-emitting $^4I_{11/2}$ level of Er^{3+} in core-only NCs (filled circles) and core–shell $NaYF_4$ NCs (open circles) doped with 2% Er^{3+} and dispersed in different solvents, as determined from single-exponential fits. Gray lines are iso-quantum-yield contours plotting $\eta \approx \Gamma_{rad}(n)/\langle\Gamma_{tot}\rangle$, based on the bulk decay rate (black cross). (b) Photoluminescence decay curves of the near-infrared emission from core-only (blue) and core–shell (red) $NaYF_4$:2% Er^{3+} NCs dispersed in toluene. Inset is a zoom-in. Solid lines show an attempt to fit our solvent-quenching model (eq 5) to the experiments using one value for ρC. (c) Same as in (a), but for the $^2F_{5/2}$ level of Yb^{3+}. Filled symbols represent core-only NCs, open symbols core–shell NCs. The NCs have dopant concentrations of 0.1% Yb^{3+} (squares), 18% Yb^{3+} (triangles), or 2% Er^{3+} plus 18% Yb^{3+}(diamonds). The Er^{3+} and Yb^{3+} emissions cannot be spectrally distinguished for the co-doped NCs, so the recorded signal will contain contributions from both. The iso-quantum-yield contours are based on the bulk decay rate of Yb^{3+} (black cross). (d) A cartoon of rapid energy transfer and energy back-transfer between Er^{3+} and Yb^{3+} centers. (e) Photoluminescence decay curves of the near-infrared Yb^{3+} emission in NCs doped with 0.1% Yb^{3+} (red), 18% Yb^{3+} (green), or co-doped with 2% Er^{3+} and 18% Yb^{3+} (blue). The signal recorded from the co-doped NCs consists for a small part of $^4I_{11/2}$ emission from Er^{3+} ions. This constitutes an estimated <5% of the total emission, based on the elemental ratio 2/18 and the ratio of radiative decay rates (Figure S2).

dependent on the NC geometry (core-only *versus* core–shell). Clearly, the Yb^{3+} luminescence is quenched by some pathway involving the NC surface that becomes more efficient at higher doping concentration. Undercoordinated Yb^{3+} centers at the NC surface could be possible quenching sites, explaining the strong concentration dependence of quenching (compare core-only NCs with 0.1% and 18% Yb^{3+}). Higher Yb^{3+} concentrations would simultaneously increase the number of such defect sites per NC and enable energy migration toward them. Co-doping Er^{3+} and Yb^{3+} is likely to lead to rapid energy transfer and energy back-transfer between the nearly resonant Yb^{3+}:$^2F_{5/2}$ and Er^{3+}:$^4I_{11/2}$ levels (Figure 4d). As a result, the effective energy migration is enhanced, and the strong quenching pathways of Er^{3+} (likely by coupling to OH-vibrations; see above) become available to the Yb^{3+} excited state. This explains why the decay rate of near-infrared excited states in NCs co-doped with 2% Er^{3+} plus 18% Yb^{3+} is enhanced by a factor 2 compared to those doped with only 18% Yb^{3+} (Figure 4c). The luminescence decay curves of the near-infrared emissions at high dopant concentrations are close to single-exponential (Figure 4e). This confirms that fast migration averages out the inhomogeneities in decay pathways between the luminescent centers (*e.g.*, those near the NC surface *versus* those in the center), resulting in one "effective" decay rate for all centers.[43]

DISCUSSION

In Figure 5 we summarize the quantum yields of the various emitting levels involved in UC by the Er^{3+}–Yb^{3+} couple in $NaYF_4$ NCs, as a function of shell thickness, doping concentration, and solvent. The data points represent experimental quantum yields determined by integrating the experimental photoluminescence decay curves:[34]

$$\eta = \Gamma_{rad}\int_0^\infty \frac{I(t)}{I(0)}dt \qquad (12)$$

where $I(0)$ is the photoluminescence intensity at $t = 0$ and Γ_{rad} is the radiative decay rate of the emitting level, estimated from the decay rate in bulk $NaYF_4$ (Figure S2) and correcting for solvent refractive index (eq 3). Similarly, the lines are predictions of our model including solvent quenching and cross-relaxation, obtained by integrating the theoretical decay curves (eq 5 or 10) for UC NCs with a core diameter of 20 nm. The model reproduces the increase in quantum yield with increasing shell thickness (open *versus* filled symbols) and with increasing solvent refractive index [from hexane (red) to chlorobenzene (blue) to carbon disulfide (gray)]. It predicts that, because of strong solvent quenching, the quantum yield of the red luminescence can be further increased with even thicker shells than we used in the experiments presented here (requiring up to 20 nm thickness for 95% luminescence quantum yield, depending on the solvent). For the green Er^{3+} emission, our model reproduces the dependence on dopant concentration [0.1% Er^{3+} (circles) *versus* 2% Er^{3+} plus 18% Yb^{3+} (squares)]. The red-emission quantum yield does not show a significant dependence on doping concentration, because it is not quenched by cross-relaxation or energy migration. On the other hand, strong quenching due to cross-relaxation causes the quantum yield of the green emission in high-doping NCs to saturate at approximately 20% for shells >3 nm. Qualitatively, it is clear that the near-infrared Yb^{3+} emission becomes more efficient with increasing shell thickness, with increasing solvent refractive index, and with lower doping concentration. However, we cannot model this quantitatively because this emission is quenched by other mechanisms than dipole–dipole coupling to solvent vibrations.

To get an idea of what our results imply for the efficiency of UC luminescence from $NaYF_4$ NCs, we consider a simplified three-level model for the UC process (Figure 5d).[48] In reality Er^{3+}–Yb^{3+}-based UC is of course much more complex, involving more energy levels and multiple energy-transfer pathways depending on excitation power.[49] Our simplified model consists of a ground state '0', a first excited state "NIR"

DOI: 10.1021/acsnano.8b01545
ACS Nano 2018, 12, 4812–4823

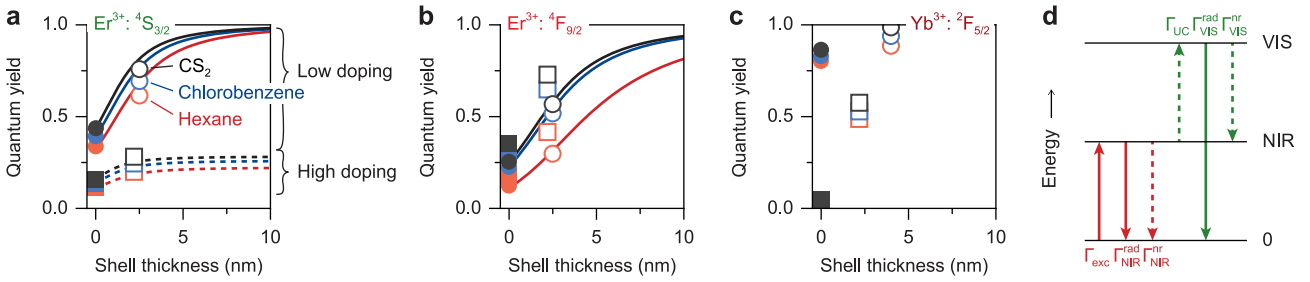

Figure 5. (a–c) The quantum yields of the various emitting levels in $NaYF_4$:Er^{3+},Yb^{3+} UC NCs as a function of shell thickness. We consider (a) the green Er^{3+} emission from the $^4S_{3/2}$ level, (b) the red Er^{3+} emission from the $^4F_{9/2}$ level, and (c) near-infrared Yb^{3+} emission from the $^2F_{5/2}$ level. Data points are obtained by integrating experimental photoluminescence decay curves (eq 12) from core-only NCs (filled symbols) or core–shell NCs (open symbols). We compare NCs dispersed in hexane (red), chlorobenzene (blue), and carbon disulfide (gray) and NCs doped with low concentration of the active center (0.1%; circles) to NCs co-doped with 2% Er^{3+} and 18% Yb^{3+} (squares). Lines are predictions from our solvent-quenching model for the green- and red-emitting levels at low doping (solid lines) and high doping (dashed lines; only distinct for the green emission). (d) Simplified model of UC with a ground state (0), an intermediate excited state (NIR), and a highest excited state (VIS). Arrows indicate excitation, decay, and energy-transfer processes.

in the near-infrared, and a second excited state "VIS" that can emit visible photons. Excitation into the intermediate level and energy-transfer UC to the highest excited state, with rate constants Γ_{exc} and Γ_{UC}, respectively, in combination with radiative and nonradiative decay of the states NIR and VIS lead to the following set of rate equations:

$$\frac{dN_{NIR}}{dt} = \Gamma_{exc}N_0 - \Gamma^{tot}_{NIR}N_{NIR} - \Gamma_{UC}N^2_{NIR} + \Gamma^{nr}_{VIS}N_{VIS} \quad (13)$$

$$\frac{dN_{VIS}}{dt} = \Gamma_{UC}N^2_{NIR} - \Gamma^{tot}_{VIS}N_{VIS} \quad (14)$$

where N_{NIR} and N_{VIS} are the populations in the intermediate and in the highest excited state, and Γ^{tot}_i denotes the total decay rate (radiative + nonradiative) of state i. The visible UC luminescence is proportional to $I_{UC} \propto \Gamma^{rad}_{VIS}N_{VIS}$. Solving the rate equations for steady-state conditions yields for the UC luminescence to second order in $\Gamma_{exc}/\Gamma^{tot}_{NIR}$, that is, in the limit of weak excitation, that

$$I_{UC} \propto \frac{\Gamma^{rad}_{VIS}\Gamma_{UC}\Gamma^2_{exc}}{\Gamma^{tot}_{VIS}(\Gamma^{tot}_{NIR})^2} = \left(\frac{\eta_{NIR}}{\Gamma^{rad}_{NIR}}\right)^2 \eta_{VIS}\Gamma^2_{exc} \quad (15)$$

We see that the UC intensity is quadratically dependent on the quantum yield η_{NIR} of the intermediate near-infrared-emitting level and linearly on the quantum yield η_{VIS} of the highest visible-emitting level. We thus conclude that the major contribution to low UC efficiencies in NCs compared to bulk material[10,11,19,20] comes from losses in the near-infrared, in line with the interpretation of Hossan *et al.*,[49] not only because the near-infrared-emitting levels are quenched strongly at high doping concentrations (Figure 5c) but also because losses in the infrared affect the overall UC intensity more strongly than losses in the visible. Shell growth improves the quantum yields in the near-infrared at high doping concentration by as much as a factor ~10 in our experiments (Figure 5c), which translates into a ~100 increase in UC intensity according to eq 15. Additionally, the shell improves the UC intensity further by a smaller factor ~2 by increasing the quantum yield in the visible (depending on the color considered and on the solvent; Figure 5a,b). The beneficial effect of shell growth on the UC intensities thus comes mainly from the inhibition of quenching in the near-infrared. We ascribe residual quenching in the infrared in core–shell NCs with a 3 nm shell to coupling of the $^4I_{11/2}$ level of Er^{3+} to OH-vibrations of embedded hydroxide ions, which can potentially be prevented with improved synthesis procedures that avoid hydroxides and water.[20] The $Yb^{3+2}F_{5/2}$ level is indirectly quenched by the same pathway, because at high doping concentrations the $Yb^{3+2}F_{5/2}$ and $Er^{3+4}I_{11/2}$ levels rapidly exchange energy by transfer and back-transfer. Quenching of the red-emitting $^4F_{9/2}$ level of Er^{3+} is due to solvent quenching and can be further suppressed with thicker shells (solid lines in Figure 5b) than the 3 nm we consider here or by excluding high-energy vibrations in the environment. Quenching of the green-emitting $^4S_{3/2}$ and $^2H_{11/2}$ levels at high doping concentration relevant to UC is mainly due to cross-relaxation to Er^{3+} neighbors (blue and yellow pathways in Figure 3c) and cannot be avoided by growing thicker shells. Indeed, also bulk material suffers from this loss pathway (Figure S5).[6]

Our systematic analysis of the decay dynamics of the various levels involved in Er^{3+}–Yb^{3+}-based UC provides important insights into the quenching pathways relevant to UC. However, many additional effects have to be considered for a full quantitative understanding of UC under all experimental conditions. For example, some studies have proposed complex population pathways for the red-emitting level, involving multiple multiphonon and/or energy-transfer processes.[35−37] Moreover, at high excitation powers the state populations can saturate, and levels higher in energy than the green- or red-emitting ones become involved in the energy-transfer and cross-relaxation pathways.[15,50] It is also important to consider that cross-relaxation and nonradiative recombination steps may not necessarily lead to irreversible energy loss, but the energy may be used in a next energy-transfer UC step. Further, the quantum yields of near-infrared and visible emission of a particular Er^{3+} center may be correlated, for example, if it is located near the NC surface.[49] This and other variations of and correlations between the rates of various UC steps can only be taken into account fully with a microscopic theoretical model that considers individual luminescent centers (*e.g.*, Er^{3+} and Yb^{3+}) explicitly,[51] as an alternative to the more common mean-field models.[35,52]

CONCLUSION

In summary, we have presented a detailed study on the excited-state dynamics in $NaYF_4$ upconversion nanocrystals co-doped with Er^{3+} and Yb^{3+}. By systematically varying important

DOI: 10.1021/acsnano.8b01545
ACS Nano 2018, 12, 4812–4823

parameters such as doping concentration and the nature of the solvent, we were able to identify quenching pathways and energy-transfer processes responsible for the reduced upconversion efficiency in nanocrystals. A microscopic model was developed to provide quantitative insight in the contribution of quenching by molecular vibrations (ligands, solvent) and cross-relaxation processes. For the green and red Er^{3+} emission, the model accurately reproduces the observed decay dynamics and also demonstrates how the solvent quenching strength depends on resonances between solvent vibrational modes and electronic transitions on the Er^{3+} ion. Growing an undoped shell around the upconversion core reduces solvent quenching, and with the model the shell thickness required for a near-complete suppression of solvent quenching can be determined. For the near-infrared emission, the agreement between the observed excited-state dynamics and our model is not satisfactory. The systematic deviation indicates the presence of an additional quenching process. Based on the resonance of the O-H stretch vibrational energy and a transition on Er^{3+} for the IR emitting level, we propose that OH^- incorporated on F^- sites in $NaYF_4$ nanocrystals is responsible. For core−shell nanocrystals, the most significant improvement in upconversion efficiency can be achieved by suppressing quenching of the near-infrared-emitting level which may be realized by alternative synthesis strategies that prevent incorporation of OH^- in the $NaYF_4$ lattice.

METHODS

Nanocrystal Synthesis. The $NaYF_4$ core nanocrystals (NCs) doped with Er^{3+} and/or Yb^{3+} were synthesized following the procedure from ref 53 with modifications based on ref 54. A mixture of $REAc_3$ (4 mmol; with RE = Y, Er, Yb in the desired ratio) in oleic acid (24 mL) and 1-octadecene (68 mL) was degassed at 120 °C under vacuum for 90 min and then allowed to cool down to room temperature under nitrogen atmosphere. A solution of NaOH (10 mmol) and NH_4F (16 mmol) in methanol (40 mL) was injected into the reaction mixture under nitrogen, which was then stirred overnight at room temperature. Next, the methanol was removed by evaporation at 100 °C under vacuum for 30 min. The reaction mixture was then quickly heated to 300 °C for 110 min under nitrogen atmosphere while stirring, during which the $NaYF_4$ NCs form. After cooling down, the NCs were washed three times by precipitation with ethanol, centrifugation, and redispersing them in cyclohexane. In the second to last washing step, a mixture of cyclohexane (12 mL) and oleic acid (12 mL) was used to redisperse the NCs to increase ligand coverage of the surface and improve the colloidal stability. The final product was dispersed in approximately 12 mL of cyclohexane.

Core−shell NCs were synthesized by growing a nonluminescent $NaYF_4$ shell around (co)doped cores using the method of ref 54. A solution of YAc_3 (1.5 mmol) in oleic acid (9 mL) and 1-octadecene (25.5 mL) was degassed at 120 °C under vacuum for 60 min. The temperature was then decreased to 80 °C under nitrogen, and 5.5 nmol of core particles was added (estimated from transmission electron microscopy and the dry weight of the cyclohexane stock dispersion). Cyclohexane was removed at 100 °C under vacuum. The reaction mixture was then allowed to cool down to room temperature, a solution of NaOH (3.75 mmol) and NH_4F (6 mmol) in methanol (15 mL) was added, and the mixture was stirred overnight. Next, methanol was evaporated at 100 °C under vacuum for 10 min. The reaction mixture was then quickly heated to 300 °C under nitrogen for 120 min before cooling down to room temperature. The NCs were washed three times by precipitation with ethanol, centrifugation, and redispersing them in cyclohexane. In the second to last washing step, a mixture of cyclohexane (3 mL) and oleic acid (3 mL) was used to redisperse the NCs to increase ligand coverage of the surface and improve the colloidal stability. The final product was dispersed in approximately 1.7 mL of cyclohexane.

Microcrystalline powders of (co)doped β-$NaYF_4$ were prepared as described in ref 5.

Spectroscopic Experiments. Photoluminescence decay dynamics of the various Er^{3+} and Yb^{3+} emissions were recorded using an Edinburgh Instruments FLS920 fluorescence spectrometer. The samples were excited with 10 ns pulses (20 Hz) from a color-tunable optical parametric oscillator (OPO) system (Opotek HE 355 II) pumped by the third harmonic of a Nd:YAG laser. The luminescence was detected with a Hamamatsu H74220−60 photomultiplier tube for visible wavelength or with a N_2-cooled R5507-73 photomultiplier tube for the near-infrared. To measure the decay dynamics of a certain energy level, we tuned the excitation laser on the same level but a few nm blue-shifted from the detection wavelength, except for the green emission where we excited in the $^2H_{11/2}$ level and detected emission from the $^4S_{3/2}$ level. These levels are thermally coupled and show the same decay dynamics.[44] To minimize reabsorption of emitted light, the NCs were dispersed in an organic solvent at low concentration, while the microcrystalline powders were diluted with white $BaSO_4$ powder, typically to 1% w/w or lower.

ASSOCIATED CONTENT

Supporting Information

The Supporting Information is available free of charge on the ACS Publications website at DOI: 10.1021/acsnano.8b01545.

Tranmission electron microscopy of the upconversion nanocrystals, photoluminescence decay of bulk material, and a complete data set and modeling of excited-state decay dynamics of the visible-emitting levels (PDF)

AUTHOR INFORMATION

Corresponding Author

*E-mail: a.meijerink@uu.nl.

ORCID

Freddy T. Rabouw: 0000-0002-4775-0859
P. Tim Prins: 0000-0002-8258-0074
Andries Meijerink: 0000-0003-3573-9289

Notes

The authors declare no competing financial interest.

ACKNOWLEDGMENTS

The work was supported by The Netherlands Center for Multiscale Catalytic Energy Conversion (MCEC), an NWO Gravitation programme funded by the Ministry of Education, Culture and Science of the government of The Netherlands. F.T.R. acknowledges financial support from The Netherlands Organisation for Scientific Research NWO (VENI grant number 722.017.002). P.V.-D. acknowledges financial support from the Swiss National Science Foundation SNSF (grant number P2BEP2_172238). We are grateful to R. Brechbühler for critical reading of the manuscript.

REFERENCES

(1) Cao, X.; Hu, B.; Zhang, P. High Upconversion Efficiency from Hetero Triplet−Triplet Annihilation in Multiacceptor Systems. *J. Phys. Chem. Lett.* **2013**, *4*, 2334−2338.

(2) Wu, M.; Congreve, D. N.; Wilson, M. W. B.; Jean, J.; Geva, N.; Welborn, M.; Van Voorhis, T.; Bulović, V.; Bawendi, M. G.; Baldo, M. A. Solid-State Infrared-to-Visible Upconversion Sensitized by Colloidal Nanocrystals. *Nat. Photonics* **2016**, *10*, 31−34.

(3) Deutsch, Z.; Neeman, L.; Oron, D. Luminescence Upconversion in Colloidal Double Quantum Dots. *Nat. Nanotechnol.* **2014**, *8*, 649−653.

DOI: 10.1021/acsnano.8b01545
ACS Nano 2018, 12, 4812−4823

(4) Makarov, N. S.; Lin, Q.; Pietryga, J. M.; Robel, I.; Klimov, V. I. Auger Up-Conversion of Low-Intensity Infrared Light in Engineered Quantum Dots. *ACS Nano* **2016**, *10*, 10829−10841.
(5) Krämer, K. W.; Biner, D.; Frei, G.; Güdel, H. U.; Hehlen, M. P.; Lüthi, S. R. Hexagonal Sodium Yttrium Fluoride Based Green and Blue Emitting Upconversion Phosphors. *Chem. Mater.* **2004**, *16*, 1244−1251.
(6) Suyver, J. F.; Grimm, J.; van Veen, M. K.; Biner, D.; Krämer, K. W.; Güdel, H. U. Upconversion Spectroscopy and Properties of $NaYF_4$ Doped with Er^{3+}, Tm^{3+} and/or Yb^{3+}. *J. Lumin.* **2006**, *117*, 1−12.
(7) Martín-Rodríguez, R.; Fischer, S.; Ivaturi, A.; Froehlich, B.; Krämer, K. W.; Goldschmidt, J. C.; Richards, B. S.; Meijerink, A. Highly Efficient IR to NIR Upconversion in $Gd_2O_2S:Er^{3+}$ for Photovoltaic Applications. *Chem. Mater.* **2013**, *25*, 1912−1921.
(8) Heer, S.; Kömpe, K.; Güdel, H.-U.; Haase, M. Highly Efficient Multicolour Upconversion Emission in Transparent Colloids of Lanthanide-Doped $NaYF_4$ Nanocrystals. *Adv. Mater.* **2004**, *16*, 2102−2105.
(9) Boyer, J.-C.; Vetrone, F.; Cuccia, L. A.; Capobianco, J. A. Synthesis of Colloidal Upconverting $NaYF_4$ Nanocrystals Doped with Er^{3+}, Yb^{3+} and Tm^{3+}, Yb^{3+} *via* Thermal Decomposition of Lanthanide Trifluoroacetate Precursors. *J. Am. Chem. Soc.* **2006**, *128*, 7444−7445.
(10) Boyer, J.-C.; Manseau, M.-P.; Murray, J. I.; van Veggel, F. C. J. M. Surface Modification of Upconverting $NaYF_4$ Nanoparticles with PEG−Phosphate Ligands for NIR (800 nm) Biolabeling within the Biological Window. *Langmuir* **2010**, *26*, 1157−1164.
(11) Wang, F.; Wang, J.; Liu, X. Direct Evidence of a Surface Quenching Effect on Size-Dependent Luminescence of Upconversion Nanoparticles. *Angew. Chem., Int. Ed.* **2010**, *49*, 7456−7460.
(12) Wang, F.; Deng, R.; Wang, J.; Wang, Q.; Han, Y.; Zhu, H.; Chen, X.; Liu, X. Tuning Upconversion through Energy Migration in Core−Shell Nanoparticles. *Nat. Mater.* **2011**, *10*, 968−973.
(13) Zou, W.; Visser, C.; Maduro, J. A.; Pshenichnikov, M. S.; Hummelen, J. C. Broadband Dye-Sensitized Upconversion of Near-Infrared Light. *Nat. Photonics* **2012**, *6*, 560−564.
(14) Zhao, J.; Lu, Z.; Yin, Y.; McRae, C.; Piper, J. A.; Dawes, J. M.; Jin, D.; Goldys, E. M. Upconversion Luminescence with Tunable Lifetime in $NaYF_4$:Yb,Er Nanocrystals: Role of Nanocrystal Size. *Nanoscale* **2013**, *5*, 944−952.
(15) Zhao, J.; Jin, D.; Schartner, E. P.; Lu, Y.; Liu, Y.; Zvyagin, A. V.; Zhang, L.; Dawes, J. M.; Xi, P.; Piper, J. A.; Goldys, E. M.; Monro, T. M. Single-Nanocrystal Sensitivity Achieved by Enhanced Upconversion Luminescence. *Nat. Nanotechnol.* **2013**, *8*, 729−734.
(16) Chen, D.; Huang, P. Highly Intense Upconversion Luminescence in Yb/Er:$NaGdF_4$ @$NaYF_4$ Core−Shell Nanocrystals with Complete Shell Enclosure of the Core. *Dalton Trans.* **2014**, *43*, 11299−11304.
(17) Liu, Y.; Zhao, J.; Zhang, R.; Liu, Y.; Liu, D.; Goldys, E. M.; Yang, X.; Xi, P.; Sunna, A.; Lu, J.; Shi, Y.; Leif, R. C.; Huo, Y.; Shen, J.; Piper, J. A.; Robinson, J. P.; Jin, D. Tunable Lifetime Multiplexing Using Luminescent Nanocrystals. *Nat. Photonics* **2014**, *8*, 32−36.
(18) Arppe, R.; Hyppänen, I.; Perälä, N.; Peltomaa, R.; Kaiser, M.; Würth, C.; Christ, S.; Resch-Genger, U.; Schäferling, M.; Soukka, T. Quenching of the Upconversion Luminescence of $NaYF_4:Yb^{3+},Er^{3+}$ and $NaYF_4:Yb^{3+},Tm^{3+}$ Nanophosphors by Water: the Role of the Sensitizer Yb^{3+} in Non-Radiative Relaxation. *Nanoscale* **2015**, *7*, 11746−11757.
(19) Fischer, S.; Johnson, N. J. J.; Pichaandi, J.; Goldschmidt, J. C.; van Veggel, F. C. J. M. Upconverting Core−Shell Nanocrystals with High Quantum Yield under Low Irradiance: On the Role of Isotropic and Thick Shells. *J. Appl. Phys.* **2015**, *118*, 193105.
(20) Rinkel, T.; Raj, A. N.; Dühnen, S.; Haase, M. Synthesis of 10 nm β-$NaYF_4$:Yb,Er/NaYF4 Core/Shell Upconversion Nanocrystals with 5 nm Particle Cores. *Angew. Chem., Int. Ed.* **2016**, *55*, 1164−1167.
(21) Johnson, N. J. J.; He, S.; Diao, S.; Chan, E. M.; Dai, H.; Almutairi, A. Direct Evidence for Coupled Surface and Concentration Quenching Dynamics in Lanthanide-Doped Nanocrystals. *J. Am. Chem. Soc.* **2017**, *139*, 3275−3282.
(22) Hyppänen, I.; Höysniemi, N.; Arppe, R.; Schäferling, M.; Soukka, T. Environmental Impact on the Excitation Path of the Red Upconversion Emission of Nanocrystalline $NaYF_4:Yb^{3+},Er^{3+}$. *J. Phys. Chem. C* **2017**, *121*, 6924−6929.
(23) Schietinger, S.; Aichele, T.; Wang, H.-Q.; Nann, T.; Benson, O. Plasmon-Enhanced Upconversion in Single $NaYF_4:Yb^{3+}/Er^{3+}$ Co-doped Nanocrystals. *Nano Lett.* **2010**, *10*, 134−138.
(24) Han, S.; Deng, R.; Xie, X.; Liu, X. Enhancing Luminescence in Lanthanide-Doped Upconversion Nanoparticles. *Angew. Chem., Int. Ed.* **2014**, *53*, 11702−11715.
(25) Sun, Q.-C.; Mundoor, H.; Ribot, J. C.; Singh, V.; Smalyukh, I. I.; Nagpal, P. Plasmon-Enhanced Energy Transfer for Improved Upconversion of Infrared Radiation in Doped-Lanthanide Nanocrystals. *Nano Lett.* **2014**, *14*, 101−106.
(26) Fischer, S.; Kumar, D.; Hallermann, F.; von Plessen, G.; Goldschmidt, J. C. Enhanced Upconversion Quantum Yield near Spherical Gold Nanoparticles − a Comprehensive Simulation Based Analysis. *Opt. Express* **2016**, *24*, A460−A475.
(27) Yin, Z.; Li, H.; Xu, W.; Cui, S.; Zhou, D.; Chen, X.; Zhu, Y.; Qin, G.; Song, H. Local Field Modulation Induced Three-Order Upconversion Enhancement: Combining Surface Plasmon Effect and Photonic Crystal Effect. *Adv. Mater.* **2016**, *28*, 2518−2525.
(28) Zhou, D.; Liu, D.; Xu, W.; Yin, Z.; Chen, X.; Zhou, P.; Cui, S.; Chen, Z.; Song, H. Observation of Considerable Upconversion Enhancement Induced by $Cu_{2-x}S$ Plasmon Nanoparticles. *ACS Nano* **2016**, *10*, 5169−5179.
(29) Xu, W.; Chen, X.; Song, H. Upconversion Manipulation by Local Electromagnetic Field. *Nano Today* **2017**, *17*, 54−58.
(30) Stouwdam, J. W.; Hebbink, G. A.; Huskens, J.; van Veggel, F. C. J. M. Lanthanide-Doped Nanoparticles with Excellent Luminescent Properties in Organic Media. *Chem. Mater.* **2003**, *15*, 4604−4616.
(31) Guyot-Sionnest, P.; Wehrenberg, B.; Yu, D. Intraband Relaxation in CdSe Nanocrystals and the Strong Influence of the Surface Ligands. *J. Chem. Phys.* **2005**, *123*, 074709.
(32) Aharoni, A.; Oron, D.; Banin, U.; Rabani, E.; Jortner, J. Long-Range Electronic-to-Vibrational Energy Transfer from Nanocrystals to Their Surrounding Matrix Environment. *Phys. Rev. Lett.* **2008**, *100*, 057404.
(33) Rabouw, F. T.; Den Hartog, S. A.; Senden, T.; Meijerink, A. Photonic Effects on the Förster Resonance Energy Transfer Efficiency. *Nat. Commun.* **2014**, *5*, 3610.
(34) Senden, T.; Rabouw, F. T.; Meijerink, A. Photonic Effects on the Radiative Decay Rate and Luminescence Quantum Yield of Doped Nanocrystals. *ACS Nano* **2015**, *9*, 1801−1808.
(35) Anderson, R. B.; Smith, S. J.; May, P. S.; Berry, M. T. Revisiting the NIR-to-Visible Upconversion Mechanism in β-$NaYF_4:Yb^{3+},Er^{3+}$. *J. Phys. Chem. Lett.* **2014**, *5*, 36−42.
(36) Berry, M. T.; May, P. S. Disputed Mechanism for NIR-to-Red Upconversion Luminescence in $NaYF_4:Yb^{3+},Er^{3+}$. *J. Phys. Chem. A* **2015**, *119*, 9805−9811.
(37) Zhang, J.; Hao, Z.; Li, J.; Zhang, X.; Luo, Y.; Pan, G. Observation of Efficient Population of the Red-Emitting State from the Green State by Non-Multiphonon Relaxation in the Er^{3+}−Yb^{3+} System. *Light: Sci. Appl.* **2015**, *4*, e239.
(38) van Dijk, J. M. F.; Schuurmans, M. F. H. On the Nonradiative and Radiative Decay Rates and a Modified Exponential Energy Gap Law for 4*f*−4*f* Transitions in Rare-Earth Ions. *J. Chem. Phys.* **1983**, *78*, 5317−5323.
(39) Sokolov, V. I.; Zvyagin, A. V.; Igumnov, S. M.; Molchanova, S. I.; Nazarov, M. M.; Nechaev, A. V.; Savelyev, A. G.; Tyutyunov, A. A.; Khaydukov, E. V.; Panchenko, V. Ya. Determination of the Refractive Index of β-$NaYF_4/Yb^{3+}/Er^{3+}/Tm^{3+}$ Nanocrystals Using Spectroscopic Refractometry. *Opt. Spectrosc.* **2015**, *118*, 609−613.
(40) Dong, C.; Pichaandi, J.; Regier, T.; van Veggel, F. C. J. M. Nonstatistical Dopant Distribution of Ln^{3+}-Doped $NaGdF_4$ Nanoparticles. *J. Phys. Chem. C* **2011**, *115*, 15950−15958.
(41) van Wijngaarden, J. T.; Scheidelaar, S.; Vlugt, T. J. H.; Reid, M. F.; Meijerink, A. Energy Transfer Mechanism for Downconversion in

DOI: 10.1021/acsnano.8b01545
ACS Nano 2018, 12, 4812−4823

the (Pr^{3+}, Yb^{3+}) Couple. *Phys. Rev. B: Condens. Matter Mater. Phys.* **2010**, *81*, 155112.
(42) Yu, D. C.; Martín-Rodrïguez, R.; Zhang, Q. Y.; Meijerink, A.; Rabouw, F. T. Multi-Photon Quantum Cutting in $Gd_2O_2S:Tm^{3+}$ to Enhance the Photo-Response of Solar Cells. *Light: Sci. Appl.* **2015**, *4*, e344.
(43) Henderson, B.; Imbusch, G. F. *Optical Spectroscopy of Inorganic Solids*; Clarendon Press: Oxford, 1989.
(44) Geitenbeek, R. G.; Prins, P. T.; Albrecht, W.; van Blaaderen, A.; Weckhuysen, B. M.; Meijerink, A. $NaYF_4:Er^{3+},Yb^{3+}/SiO_2$ Core/Shell Upconverting Nanocrystals for Luminescence Thermometry up to 900 K. *J. Phys. Chem. C* **2017**, *121*, 3503−3510.
(45) Villanueva-Delgado, P.; Biner, D.; Krämer, K. W. Judd−Ofelt Analysis of β-$NaGdF_4$: Yb^{3+}, Tm^{3+} and β-$NaGdF_4:Er^{3+}$ Single Crystals. *J. Lumin.* **2017**, *189*, 84−90.
(46) Fischer, S.; Swabeck, J. K.; Alivisatos, A. P. Controlled Isotropic and Anisotropic Shell Growth in β-$NaLnF_4$ Nanocrystals Induced by Precursor Injection Rate. *J. Am. Chem. Soc.* **2017**, *139*, 12325−12332.
(47) Wang, F.; Liu, X. Upconversion Multicolor Fine-Tuning: Visible to Near-Infrared Emission from Lanthanide-Doped $NaYF_4$ Nanoparticles. *J. Am. Chem. Soc.* **2008**, *130*, 5642−5643.
(48) Pollnau, M.; Gamelin, D. R.; Lüthi, S. R.; Güdel, H. U.; Hehlen, M. P. Power Dependence of Upconversion Luminescence in Lanthanide and Transition-Metal-Ion Systems. *Phys. Rev. B: Condens. Matter Mater. Phys.* **2000**, *61*, 3337−3346.
(49) Hossan, M. Y.; Hor, A.; Luu, Q.; Smith, S. J.; May, S.; Berry, M. T. Explaining the Nanoscale Effect in the Upconversion Dynamics of β-$NaYF_4:Yb^{3+},Er^{3+}$ Core and Core−Shell Nanocrystals. *J. Phys. Chem. C* **2017**, *121*, 16592−16606.
(50) Gargas, D. J.; Chan, E. M.; Ostrowski, A. D.; Aloni, S.; Altoe, M. V. P.; Barnard, E. S.; Sanii, B.; Urban, J. J.; Milliron, D. J.; Cohen, B. E.; Schuck, P. J. Engineering Bright Sub-10-nm Upconverting Nanocrystals for Single-Molecule Imaging. *Nat. Nanotechnol.* **2014**, *9*, 300−305.
(51) Villanueva-Delgado, P.; Krämer, K. W.; Valiente, R.; de Jong, M.; Meijerink, A. Modeling Blue to UV Upconversion in β-$NaYF_4:Tm^{3+}$. *Phys. Chem. Chem. Phys.* **2016**, *18*, 27396−27404.
(52) Fischer, S.; Steinkemper, H.; Löper, P.; Hermle, M.; Goldschmidt, J. C. Modeling Upconversion of Erbium Doped Microcrystals Based on Experimentally Determined Einstein Coefficients. *J. Appl. Phys.* **2012**, *111*, 013109.
(53) Li, Z.; Zhang, Y. An Efficient and User-Friendly Method for the Synthesis of Hexagonal-Phase $NaYF_4$:Yb, Er/Tm Nanocrystals with Controllable Shape and Upconversion Fluorescence. *Nanotechnology* **2008**, *19*, 345606.
(54) Wang, F.; Deng, R.; Liu, X. Preparation of Core-Shell $NaGdF_4$ Nanoparticles Doped with Luminescent Lanthanide Ions to Be Used as Upconversion-Based Probes. *Nat. Protoc.* **2014**, *9*, 1634−1644.

DOI: 10.1021/acsnano.8b01545
ACS Nano 2018, 12, 4812−4823